Special Collection: Papers from the 14th International Symposium on Atomic Level Characterizations for New Materials and Devices (ALC '22)

C. Tusche ⁽ⁱ⁾; K. Hagiwara ⁽ⁱ⁾; X. L. Tan ⁽ⁱ⁾; Y.-J. Chen ⁽ⁱ⁾; C. M. Schneider ⁽ⁱ⁾



J. Vac. Sci. Technol. B 41, 042201 (2023) https://doi.org/10.1116/6.0002707





CrossMark

Related Content

Assignment of the Ultraviolet Mystery Band of Olefins

J. Chem. Phys. (May 2004)

Interpretive principles and the quantum mysteries

American Journal of Physics (November 1998)

A More Challenging Mystery Tube for Teaching the Nature of Science

Phys. Teach. (May 2019)





Exploring the mysteries of topology in quantum materials by spin-resolved spectroscopies (1)

Cite as: J. Vac. Sci. Technol. B 41, 042201 (2023); doi: 10.1116/6.0002707

Submitted: 22 March 2023 · Accepted: 10 May 2023 ·

Published Online: 31 May 2023







C. Tusche, ^{1,2} 📵 K. Hagiwara, ³ 📵 X. L. Tan, ¹ 📵 Y.-J. Chen, ^{1,2} 📵 and C. M. Schneider ^{1,2,4,a)} 📵 **AFFILIATIONS**

¹Peter Grünberg Institute, Research Center Jülich, D-52425 Jülich, Germany

- ²Physics Department, University Duisburg-Essen, D-47057 Duisburg, Germany
- ³Institute for Molecular Science, Okazaki Aichi 444-0867, Japan
- ⁴Physics Department, University of California, Davis, Davis, California 95616

Note: This paper is a part of the Special Topic Collection: Papers from the 14th International Symposium on Atomic Level Characterizations for New Materials and Devices (ALC 22).

a)Author to whom correspondence should be addressed: c.m.schneider@fz-juelich.de

ABSTRACT

Materials with unique quantum characteristics–quantum materials—have become of great importance for information technology. Among others, their unique transport phenomena are in many cases closely connected to details of the electronic structure. Exploring the electronic states and the interplay of the interactions in this material class down to the electron spin is, therefore, mandatory to understand and further design their physical behavior. We discuss several quantum materials studied by an advanced photoelectron spectroscopy further design their physical behavior. We discuss several quantum materials studied by an advanced photoelectron spectroscopy approach—spin-resolved momentum microscopy with tunable synchrotron radiation—and illustrate the role of a progressive symmetry reduction leading to particular features of their electronic structures observed in the experiment. reduction leading to particular features of their electronic structures observed in the experiment.

© 2023 Author(s). All article content, except where otherwise noted, is licensed under a Creative Commons Attribution (CC BY) license (http://creativecommons.org/licenses/by/4.0/). https://doi.org/10.1116/6.0002707

I. INTRODUCTION

With the breakdown of Moore's law, the search for alternative concepts to store and process data in information technology has greatly intensified. This includes the exploration of new state variables beyond the electron charge, such as the electron spin, various defects, collective states, correlations, etc. The ongoing evolution initiated several research fields to employ these state variables, such as spintronics, topotronics, valleytronics, orbitronics, and others. Beyond the traditional digital computing approaches, there are also several developments of these concepts into neuromorphic computing and quantum computing underway, provided their quantum properties can be adequately exploited.

The broad-ranged evolution in information technology extensively explores also novel material systems. This involves particularly so-called quantum materials, which are considered a key resource for the 21st century, taking us from the silicon age into the "quantum age." Quantum materials promise a wealth of novel phenomena with respect to electrical transport, superconductivity,

magnetism, or multiferroicity. Often, their electronic properties are linked to nongeneric quantum effects, which are caused by topology or chirality.

One characteristic feature of emergent or quantum materials is the competition of various spin-dependent interactions, such as spin-orbit coupling and exchange interaction. The simplest quantum material in this respect may be a classical ferromagnet, i.e., Fe, Co, or Ni. Although in such a material, spin-orbit coupling is usually considerably smaller than the exchange interaction, it leads to distinct quantum phenomena, such as the magnetocrystalline anisotropy affecting the global spatial orientation of the magnetization, or hybridization and spin-mixing effects in the electronic structure.8 As we will see below, even such a system may reveal topological properties under the right conditions.

In addition, depending on the material system, there may be a breaking of inversion symmetry and/or time-reversal symmetry at play. As a result, topological materials can range from metals to insulators. In the vicinity of the Fermi level E_F , this situation leads to peculiar relativisticlike linear dispersions of the electronic states.

This is, in part, due to the relativistic nature of the spin-orbit interaction, which may also result in band inversion phenomena close to E_F . In momentum space, we, therefore, observe cone-shaped structures, such as the ones depicted in Fig. 1(a). In the simplest case, these cone-shaped features are called Dirac cones. They emerge from a Dirac point with the cone axis aligned with k_z (e.g., rotational symmetry around k_z in the case of graphene) and the lower (upper) cone half corresponding to valence (conduction) electron states. This "type-I" Dirac configuration may be changed by anisotropies in the crystalline or electronic structure, which usually tilt the cone axis away from k_z [Fig. 1(a), center]. If the tilt is high enough, in fact, electron and hole pockets are formed and the resulting "type-II" Dirac node is located at their boundary [Fig. 1(a), right]. These type-II Dirac semimetals still preserve spatial and time reversal symmetries and are characterized by a so-called topological quantum number or charge C = 0. However, breaking one of them, the Dirac nodes split into two constituent Weyl nodes, and the material becomes a Weyl semimetal with a topological charge C = 1 [Fig. 1(b)]. In addition, the two Weyl nodes possess defined opposite chiralities and are connected

energy reduction electron pocket

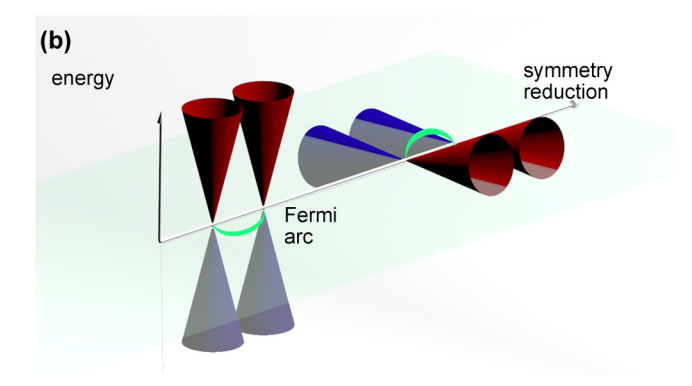


FIG. 1. Development of Dirac (a) and Weyl cones (b). The cones may tilt in the k-space, which is caused by, e.g., a lower crystal symmetry. For strong tilting (e.g., NiTe₂), the cones are intersecting the k_x – k_y plane, causing the formation of electron and hole pockets at the Fermi surface. The Weyl cones in (b) emerge when spatial or time inversion is broken. They may be tilted as well (e.g., MoTe₂), and the Weyl nodes are connected by Fermi arcs (green) on the sample surface.

by a Fermi arc presenting a surface projection of a two-dimensional Fermi contour. In both Dirac and Weyl semimetals, the complex interplay of symmetries and interactions impacts the electronic structure by locking spin and momentum, which may cause complex spin textures in momentum space.

For reasons of completeness, we note that such materials may exhibit complex spin textures also in real space, resulting in the magnetic case in solitonic structures, such as skyrmions¹¹ or hopfions.¹²

Although this review focuses on static aspects, the application regime of spin-resolved momentum microscopy may be much wider. It can be easily extended into the time domain and may even be pushed to ultrafast experiments. We recall that the material generally involves distinct intrinsic time scales related to excitations of the lattice, the spin system, or the electron system. Within these time scales ranging from picoseconds (ps) down to a few femtoseconds (fs), we can excite equilibrium processes (adiabatic or thermal changes) but also drive nonequilibrium processes. The latter lead to transient spin or electron distributions usually

(a) real space imaging



(b) momentum space imaging

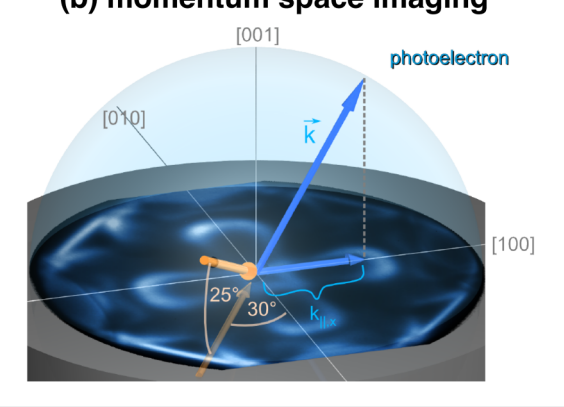


FIG. 2. Imaging modes in photoemission electron microscopy. (a) A real-space image maps the topography, chemical distribution, or magnetic structure at the surface. (b) A momentum-space image images the angular distribution of the (energy-filtered) photoelectrons in reciprocal space, resulting in a cross section through the Brillouin zone.

decaying with characteristic ps or fs time constants. This also holds for quantum materials, ¹⁴ such as the ones discussed in this review.

Beyond transient states, the additional dimension granted by the time domain offers the ability to engineer unconventional quantum states: coherent coupling of light with materials can create new photon-quasiparticle states and, thus, fundamentally change their intrinsic properties. One of the most promising examples are Floquet–Bloch states, where the coherent nature of the driving electric field of a laser is imprinted onto the electronic structure. It can be expected that these "dressed" states exhibit topological properties that are fundamentally distinct from static materials, such as proposed—but yet undiscovered—type-III Dirac cones or Floquet–Weyl states in otherwise trivial materials. 17,18

II. EXPERIMENTAL ASPECTS

A. Instrumental details

In our studies on quantum materials, we employ several advanced spin-resolved electron spectroscopies with different capabilities. ^{19,20} The most advanced—momentum microscopy—employs an energy-filtered photoelectron emission microscope (PEEM)²¹ and offers two imaging modes with a variety of contrast

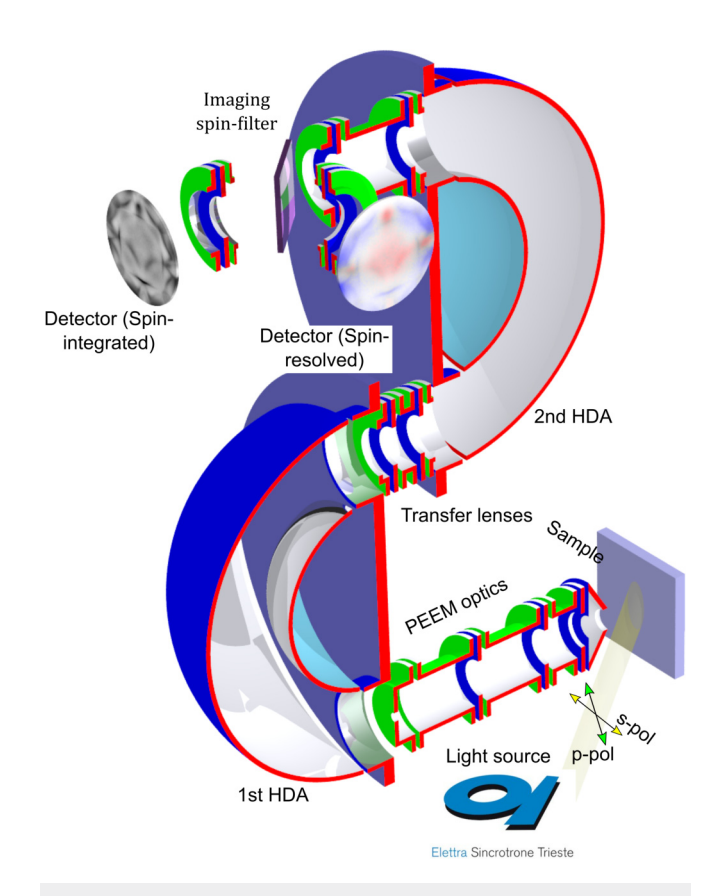


FIG. 3. Layout of the momentum microscope operated at Elettra (Italy) along with the light incidence to the sample.

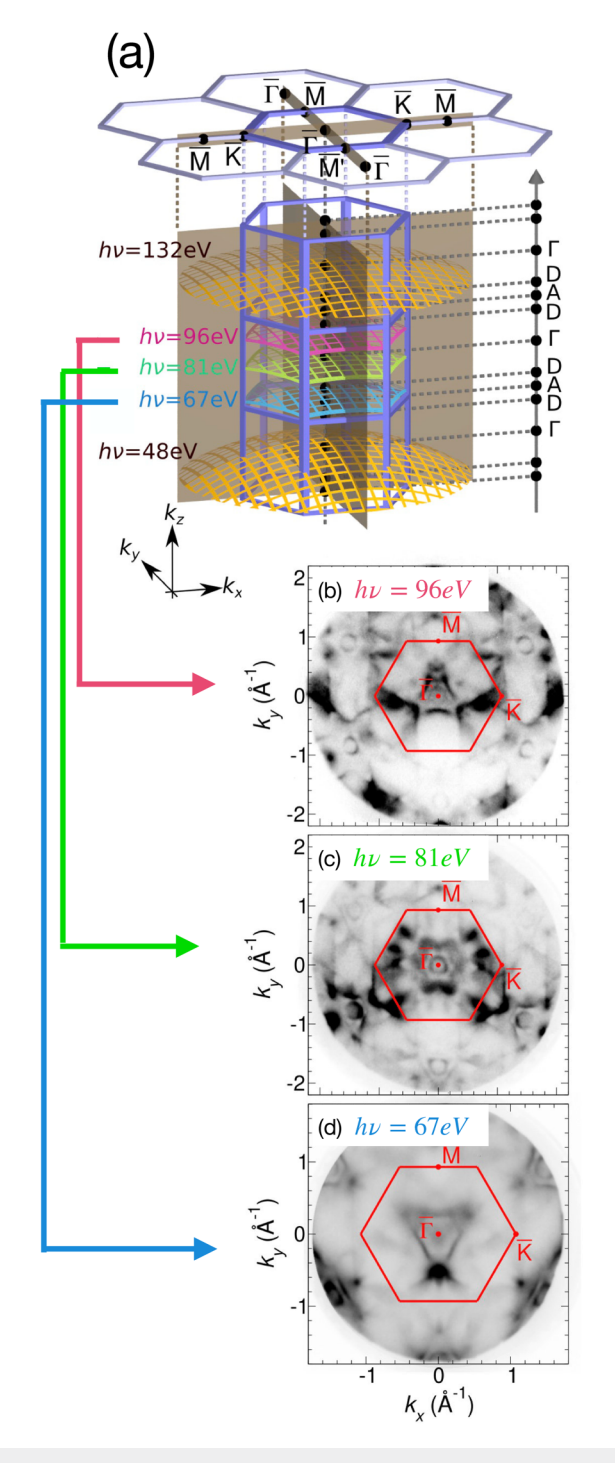


FIG. 4. Illustration of a measuring sequence in momentum microscopy for the example of a NiTe₂ crystal. The bulk Brillouin zone (symmetry labels Γ , D, A, D) and the surface projection (symmetry labels $\overline{\Gamma}$, \overline{M} , \overline{K}) are hexagonal. Each photon energy $h\nu$ probes the electronic states along a spherical cap segment (a). Momentum maps at the Fermi level ($E_B=0$) are shown for photon energies $h\nu=67$ eV (d), $h\nu=81$ eV (c), and $h\nu=96$ eV (b).



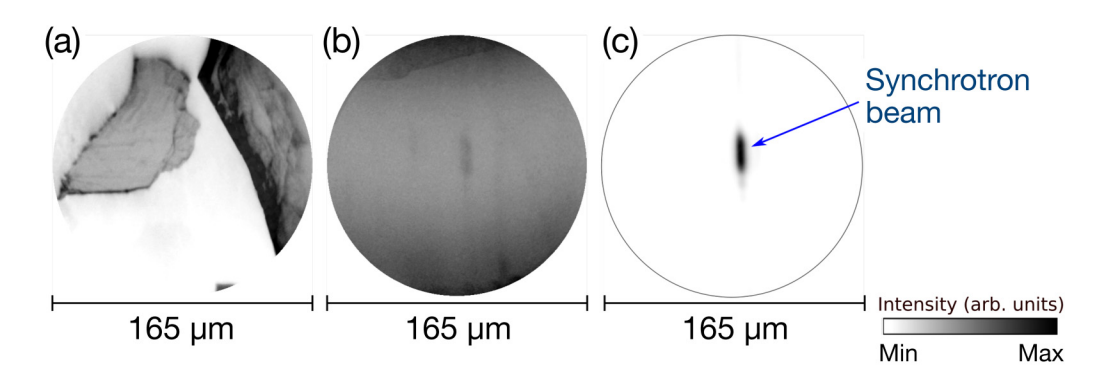


FIG. 5. Sample adjustment for momentum microscopy. (a) Real-space image of a NiTe2 crystal by a mercury discharge lamp. (b) Desired flat area for the momentum microscopy measurements. (c) The same area illuminated by the synchrotron light shows the microfocus (dark) spot.

mechanisms. In the real-space mode [Fig. 2(a)], the spatial distribution of the photoelectrons forms a magnified image showing the topography along the sample surface. If the sample is illuminated by polarized synchrotron light, one can also map the lateral distribution of chemical components or magnetic structures. In the momentum or k-space mode [Fig. 2(b)], we exploit the energyfiltering in a double-hemispherical analyzer (DHA) and directly map the angular distribution of the photoelectrons. This is usually achieved by an additional lens in the PEEM column, which performs a Fourier transform of the real-space image. The momentum image contrast results from the difference of the photoelectron flux along all momentum vectors \vec{k} in front of the sample for defined kinetic energy E_k . In this mode, a cut through the Brillouin zone maps the k-dispersion of the electronic bands.

The spin-resolved momentum microscope employed for our studies is located as a permanent end station at the nanospectroscopy beamline of the storage ring Elettra (Trieste, Italy). The general layout (Fig. 3) has been described recently. 19 The beamline delivers elliptically and linearly polarized light into a beam spot on the sample with microfocus quality, i.e., only $\sim 10 \,\mu m$. The system is also equipped with a surface science chamber to prepare and characterize clean surfaces. This also includes cleaving various types of samples, including 2D transition metal dichalcogenides. The sample stage in the microscope can be cooled down to about 100 K.

The instrument houses a two-dimensional spin filter unit, employing spin-dependent scattering from a W(001) surface placed under 45° at the exit of the DHA.²² The spin sensitivity axis is then perpendicular to the scattering plane. As has already been demonstrated, the spin-resolved operation works in both the real-space mode, e.g., for the imaging of magnetic domains,²³ and in the momentum-space mapping of electronic states.²⁴ A future upgrade envisages the change to the Au/Ir(100) spin detection scheme.²

The combination of the spin-resolved momentum microscope and the nanospectroscopy beamline provides a unique approach to all details of the electronic structure because the spin-resolved studies can be conveniently complemented by measurements of dichroic phenomena in the angular distribution of photoelectrons by circularly or linearly polarized light. 26-29 These may then be sensitive to the orbital components of the wave functions.

B. Measurement procedure

The scheme of a momentum microscopy measurement is illustrated in Fig. 4. The example chosen is that of a trigonal NiTe₂ [2D transition metal dichalcogenide (TMDC)] crystal, which will be discussed further in Sec. III. For a given photon energy hv, we obtain a full three-dimensional data set $\{E_B, k_x, k_y\}$ as a function of binding energy E_B and in-plane momentum components k_x and k_v . The photon energy defines a certain k_z -range in the bulk Brillouin zone. Due to the energy and momentum conservation in R the photoemission process, the accessible k-values lie on a curved $\frac{k}{60}$ surface, the curvature of which depends on the photon energy as indicated in the figure. In going from hv = 48 to hv = 132 eV, the cuts (colored spherical cap segments) move through several Brillouin zones along k_z . Taking only the data at the Fermi level, $\overset{\omega}{\otimes}$ i.e., $E_B = 0$, results in momentum maps (b)–(d), where we also $\frac{\infty}{5}$ include the size of the surface Brillouin zones probed with symmetry points $\overline{\Gamma}$, \overline{M} , \overline{K} . With increasing photon energy, different momentum fields of view were chosen. Depending on the photon energy, the images show three- or sixfold symmetry, whereas the first one results from linear dichroism. 30,3

The same procedure is applied for spin-resolved momentum maps, with the only difference being that the momentum map then displays the information on the orientation and magnitude of the spin vector component $P(E_B, k_x, k_y)$.

Our studies on quantum materials involved extended crystals, but also small crystallites or small flakes, e.g., from 2D transition metal dichalcogenides. The latter are often obtained by micromechanical cleavage or adhesive tape transfer onto a template, resulting only in submillimeter flat areas. In order to find these suitable areas for momentum microscopy under such conditions, we use the real-space imaging of the instrument for a search of the sample surface. For this purpose, the sample is first illuminated by a mercury discharge lamp to map the surface topography [Fig. 5(a)]. After finding a suitable flat area [Fig. 5(b)], it is placed at the position of the synchrotron beam. For comparison, the size of the microfocus synchrotron beam is shown on the same scale [Fig. 5(c)]. Therefore, in the momentum mode, the photoelectrons originate only from this illuminated $\sim 10 \,\mu m$ area.

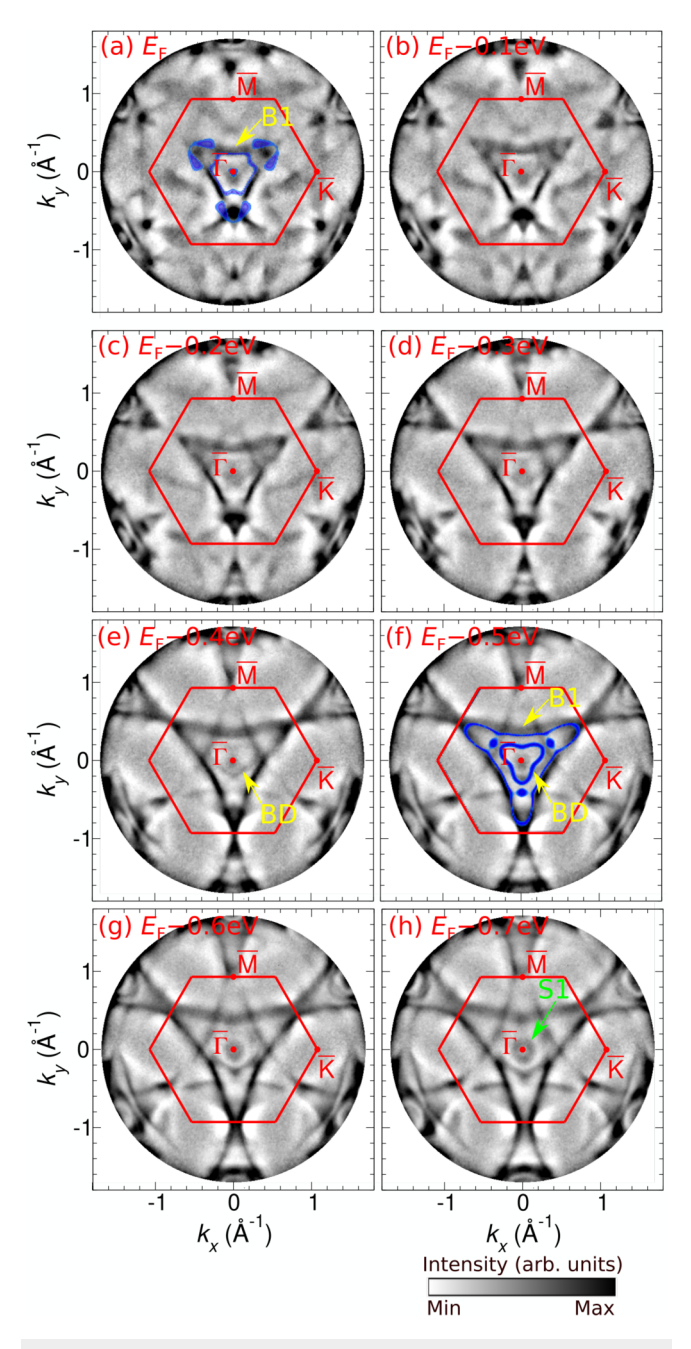


FIG. 6. Momentum maps from NiTe2 taken with linearly polarized light at $h\nu=67\,\mathrm{eV}$ as a function of increasing binding energy E_B [panels (a)-(h)] starting from the Fermi energy E_F [panel (a)]. Blue lines in panels (a) and (f) indicate calculated bulk states. (Also marked as BD and B1.)

C. Toward time domain studies

In order to enable ultrafast (i.e., fs-regime) experiments with a momentum microscope, we first need a suitable pulsed light

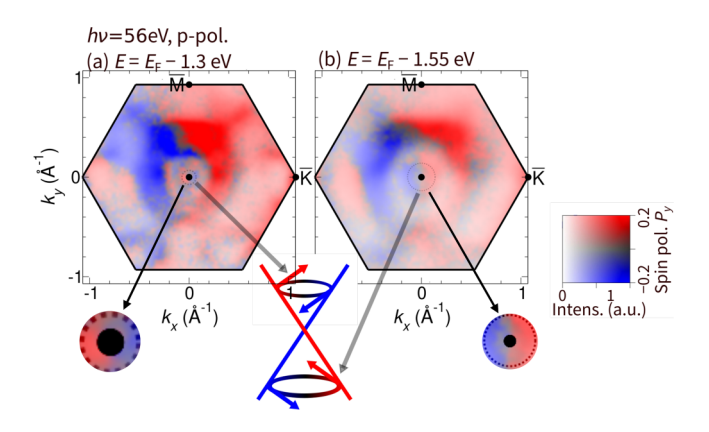


FIG. 7. Spin texture of the surface Dirac cone (circular mark) measured at $h\nu = 56$ eV. Constant binding energy maps at (a) $E_B = E_F - 1.3$ eV and (b) $E_B = E_F - 1.55 \,\mathrm{eV}$ showing the spin polarization distribution of the P_V spin component. Circular sections are magnifications of the center rings around $\overline{\Gamma}$. Lower inset: Illustration of the spin-momentum locking and the spin texture.

source. In the last decade, the development of femtosecond lasers has made steep progress. There are, on the one hand, free-electron lasers, which deliver fs-pulses over a wide range of photon energies.³² However, their limitation with respect to momentum microscopy may be too high peak intensity, thus creating space charge issues. On the other hand, there is a variety of commercial 8 Ti:Sapphire lasers, the light of which can be used to drive higher gharmonic generation (HHG) setups reaching photon energies up to gas few 100 eV. 33,34 Such systems are already involved in spina few 100 eV. 33,34 Such systems are already involved in spinresolved photoemission experiments, e.g., to explore the ultrafast 8 spin dynamics in the band structure of ferromagnets.³

Our group currently constructs and builds a dedicated HHG source for a lab-based spin-resolved momentum microscope. The driving laser operates at $\lambda = 1030 \, \text{nm}$ with a repetition frequency of 10 MHz.³⁴ The HHG process takes place in a high pressure Ar chamber, the resulting HHG radiation being guided through a beamline and a monochromator into the momentum microscope. The entire setup is designed to limit the influence of space charge effects, which otherwise may affect the energy and momentum resolution of the microscope.

III. RESULTS AND DISCUSSION

In our studies, we addressed a variety of two-dimensional material systems in order to detail the role of individual interactions and explore the gradual influence of symmetry-breaking mechanisms. This included several TMDCs, such as NiTe₂ (time reversal and inversion symmetry preserved) and MoTe₂ (inversion symmetry broken), but also "simple" ultrathin Fe films grown on W(110) (time-reversal symmetry broken).

A. NiTe₂

NiTe₂ is a so-called type-II Dirac semimetal; i.e., the Dirac cones are strongly tilted with respect to the Fermi surface resulting in the formation of electron and hole pockets. The crystal still

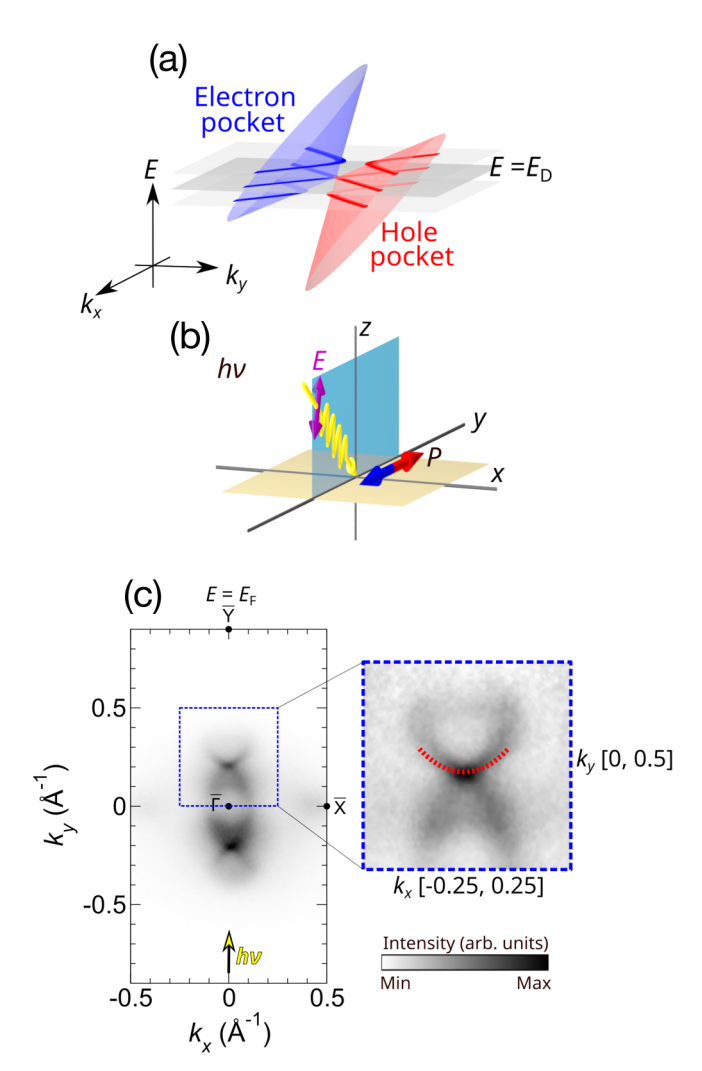


FIG. 8. Fermi-surface contour map of MoTe₂ obtained by p-polarized light of $h\nu = 52 \, \text{eV}$. (a) Geometrical orientation of one set of Weyl cones and Weyl points. (b) Experimental geometry. (c) Contour map at E_F of the Weyl cones in the k_x , k_y plane and a magnified image of the upper cone. The Weyl points are connected by a Fermi arc (curved broken line).

maintains space-inversion symmetry, and its topological phase is described by a topological charge C = 0. NiTe₂ is composed of a stack of Te-Ni-Te layers, which are bonded by van der Waals interactions. The resulting {100} surface exhibits a trigonal symmetry. Measurements were done at T = 100 K.

The variation of the NiTe₂ momentum maps (at E_F) with photon energy hv has already been shown in Fig. 4. In Fig. 6, we display the momentum maps at hv = 67 eV as a function of binding energy E_B below E_F . This reveals a detailed view of the electronic bulk and surface states in NiTe2 and their dispersion. The surface Brillouin zone with symmetry labels $\overline{\Gamma}$, \overline{M} , and \overline{K} is marked in red. The states marked in blue indicate a bulk state B1 and a bulk Dirac cone BD. The triangle shape of the structures

reveals that the states have a threefold symmetry. Further away from the Fermi level ($E_B = E_F - 0.7 \text{ eV}$), we start to see a feature with sixfold symmetry around the $\overline{\Gamma}$ -point, which stems from the surface state S1. These findings and assignments are generally in good agreement with band-structure calculations.

We can learn more about the character of the surface SD and the bulk Dirac cones BD from the photoelectron spin analysis. A result for the surface Dirac cone is shown in Fig. 7, comparing the spin-resolved photoemission intensities at a photon energy of hv = 56 eV, where the surface Dirac cone is most pronounced. When moving from binding energy $E_B = E_F - 1.3 \text{ eV}$ [Fig. 7(a)] to $E_B = E_F - 1.55$ eV [Fig. 7(b)], we probe the cone above and below the surface Dirac point. The spin polarization component P_{ν} along the y direction is represented in a red/blue color code. For both binding energies, we observe a small ringlike feature with sixfold symmetry and a quasicontinuous change of the spin polarization between red and blue (marked by small dotted rings around $\overline{\Gamma}$). We note that spin polarization along these rings reverses from (a: $+k_x$ blue) to (b: $+k_x$ red) along the k_x -line direction. This is a clear signature of spin-momentum locking in the cones similar to the one found in PdTe₂³⁷ and depicted in the inset of Fig. 7.

Our recent studies showed that under certain conditions, also, the bulk Dirac state may exhibit spin polarization in photoemission experiments. This effect is the subject of a forthcoming paper.³

B. MoTe₂

In case we further break the symmetry in the crystal, we will 8 significantly change its topology. This can be achieved, i.e., by go breaking space-inversion symmetry. We will then end up with a group of type II Word commetted in which each Direct cone splits up into type-II Weyl semimetal, in which each Dirac cone splits up into two so-called Weyl cones with topological charges $C = \pm 1$. Such a situation is found for $1T_d$ MoTe₂, being a low-temperature \approx (T < 250K) topological phase of molybdenum ditelluride. Like in $\frac{50}{2}$ the previous example of NiTe2, these Weyl cones are strongly tilted in the E, k-space, thus leading to electron and hole pockets (cf. the inset of Fig. 8). Measurements were done at T = 100K.

The momentum map at E_F (Fermi-surface contour) depicts signatures of these Weyl cones, which have been recorded by p-polarized light (Fig. 8). The hole pocket is centered around the $\overline{\Gamma}$ point, whereas two electron pockets are located above $(k_y = +.3 \text{ Å}^{-1})$ and below $(k_y = -.3 \text{ Å}^{-1})$ the Brillouin zone center. The figure also contains the Fermi arc (a red broken line guide to the eye), which connects two Weyl nodes. Further spectroscopic analysis shows the Weyl nodes to be located about +50 meV above E_F (thesis Hagiwara *et al.*³⁹).

A particular property of the Weyl cones is their intrinsic chirality, which results in a pronounced interaction with circularly polarized light. This feature is exploited in Fig. 9, which displays the circular dichroism (CDAD)⁴⁰ appearing in the momentum maps around $\overline{\Gamma}$ at and below E_F . A clear feature at $E=E_F$ is the appearance of "X"-shaped crossings at $k_y=\pm 0.2$ Å⁻¹ originating from the boundary between the hole and electron pockets. Going below the Fermi level, the crossings flatten out somewhat and are surrounded by ringlike structures of dichroic nature. This is due to the fact that we are probing more and more of the hole pockets as is explained below.

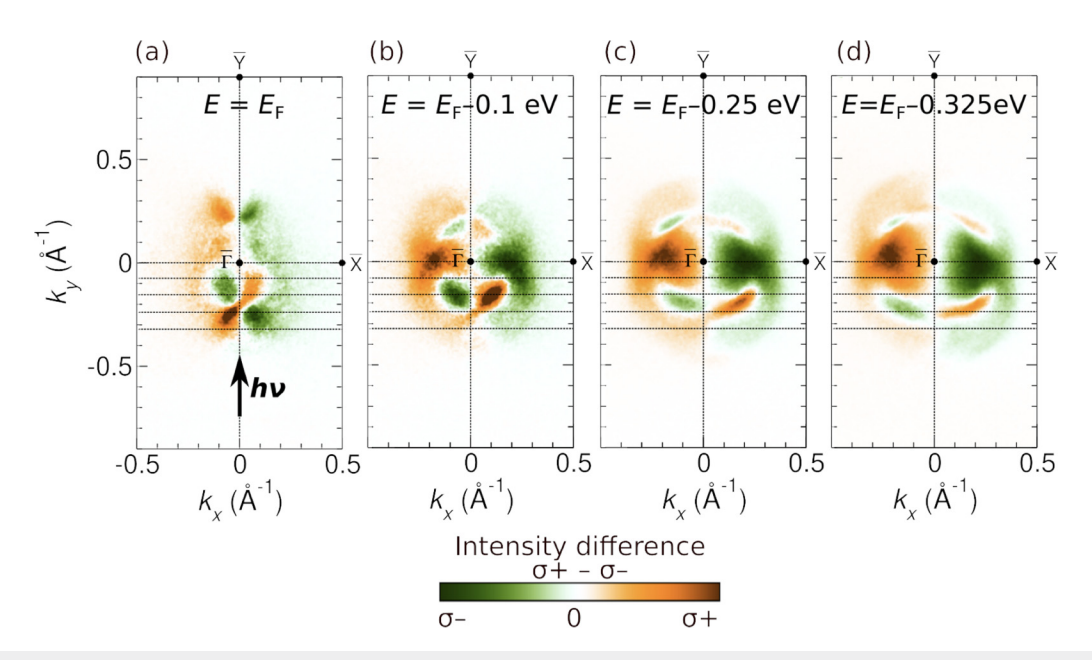


FIG. 9. Momentum distribution of the circular dichroism measured at a photon energy of $h\nu=60\,\text{eV}$. (a)–(d) Constant-energy maps at $E=E_F$ (a), $E_F-0.1\,\text{eV}$ (b), $E_F-0.25\,\text{eV}$ (c), and $E_F-0.325\,\text{eV}$ (d). Plotted intensities indicate the difference of photoemission intensities for right- (σ^+) and left- (σ^-) circularly polarized light according to the color code.

In Fig. 10, we give a schematic evolution of the corresponding band features as a function of the binding energy, the colors (green, orange) indicating the sign of the dichroism. We start with the situation above E_F where the electron pockets are located (left). Moving down in energy toward E_F , the electron and hole pockets touch each other, corresponding to the crossings observed in Fig. 9(a). Further below E_F , the crossing point broadens and opens, the constant-energy contour showing the hole pockets. The relative position of the hole bands is changed with increasing binding energy, as indicated by the circles around the former crossing points.

In addition to the chirality-induced effects observed in Fig. 9, the spin-resolved momentum microscopy also yields information on the spin texture at the crossing points. This is depicted in Fig. 11 comparing the results with s- and p-polarized light. In the case of s-polarized light (top panel), we see a similar "X"-shaped

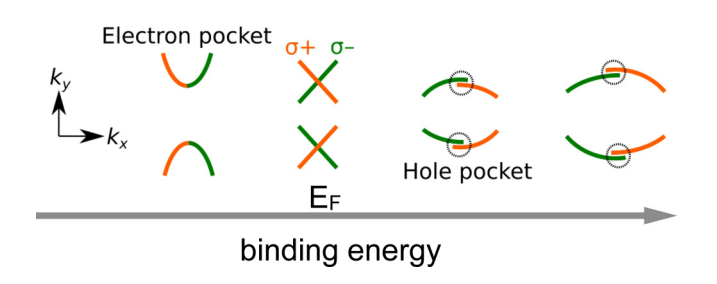


FIG. 10. Schematic band-structure development as a function of binding energy.

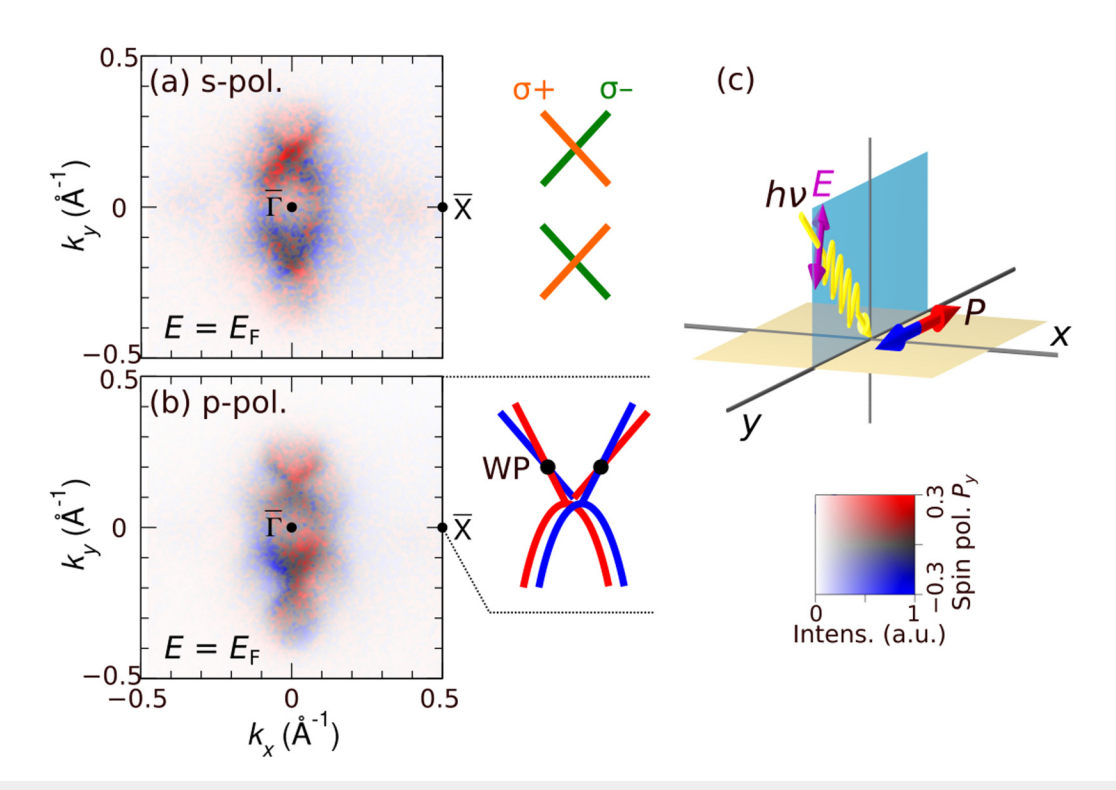
pattern in the spin texture as already observed in Fig. 9(a) in the g CDAD (reproduced on the right-hand side of the panel). The "X" reflects a simple crossing of spin-up (red) and spin-down (blue) states (polarization measured along the k_y axis).

The situation with p-polarized light (bottom panel) appears to be more complex. We recall that the spin-splitting of the Weyl cones is a result of broken inversion symmetry in the presence of SOC. As a consequence, a spin-degenerate Dirac cone splits into a pair of spin-split Weyl cones with opposite chiral charges. Indeed, p-polarized light reveals further details; i.e., the "X" contour is made up of double lines with spin-down states (blue) shifted slightly left to the spin-up states (red). A graphical sketch for the $k_y > 0$ situation is depicted on the right-hand side of the panel. Please note, however, that the spin-splitting in the spin-resolved data is too small to be resolved in spin-integrated CDAD experiments.

Why do we see different spin textures with light polarization? This has to do with the fact that the spin texture reflects the chirality of the Weyl states, and the textures related to the spin angular momentum and the orbital angular momentum (CDAD) appear different due to optical dipole selection rules.

C. Ultrathin Fe films on W(110)

Fe can be considered a "trivial" quantum material, in which the bulk exhibits ferromagnetic spin ordering below the Curie temperature T_C and also has a small spin–orbit contribution, which is responsible—among others—for the magnetocrystalline anisotropy. In recent years, we have investigated Fe films mainly with respect to the interplay of the two spin-dependent interactions on the electronic states. This situation results in a quite complex band



at hv = 52 eV with s- (a) and p-polarized light (b). Sketches (right-hand side) illuste observed CDAD texture from Fig. 10(a) using the same green and orange color obtoemission experimental geometry. The electric field vector (E) for p-polarized light a: red (spin-up) and blue intensities (spin-down photoelectrons) with a spin quantizared color reduces T_C . Second, the films are usually grown on a substrate, which means that we introduce an additional interface and via the **FIG. 11.** Spin texture of the Weyl cones. Spin-resolved Fermi-surface contours taken at hv = 52 eV with s- (a) and p-polarized light (b). Sketches (right-hand side) illustrate the observed Fermi-surface features in (k_x, k_y) . The sketch in panel (a) maps the observed CDAD texture from Fig. 10(a) using the same green and orange color code. Sketch in panel (b) refers the situation in the upper half region ($k_y > 0$). (c) Photoemission experimental geometry. The electric field vector (E) for p-polarized light is marked by a purple arrow. Spin-resolved intensities are encoded with a 2D color code: red (spin-up) and blue intensities (spin-down photoelectrons) with a spin quantization axis along k_v .

structure with distinct spin-dependent bandgaps and spin-mixing phenomena around the Fermi level.8

The situation changes drastically, however, if we consider Fe films in the monolayer limit. First, the reduced dimensionality which means that we introduce an additional interface and via the lattice mismatch also some strain. At the interface, one must consider electronic hybridization between electrons from the substrate

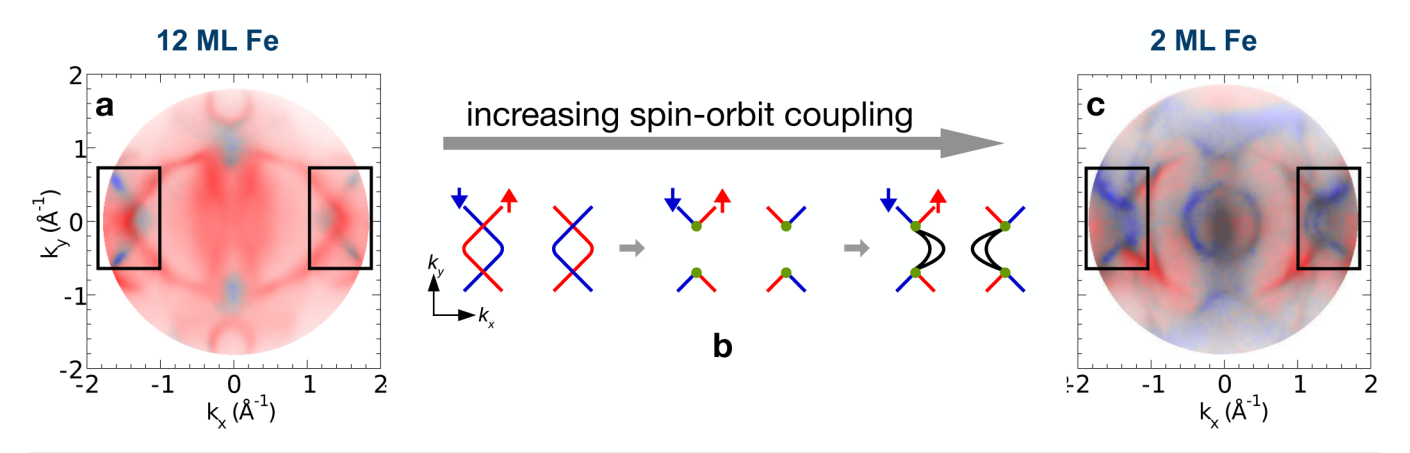


FIG. 12. Spin-resolved photoelectron momentum maps from Fe/W(110) at E_F taken at hv = 50 eV. (a) 12 monolayer Fe and (c) 2 monolayer Fe films. Sample magnetization along the -y-direction. Spin polarization color scale ranges from P=+0.7 (red) to P=-0.7 (blue). (b) Intermediate steps in the formation of Weyl points and Fermi arcs at the surface, caused by increasing spin-orbit coupling as indicated.

and film, which may lead to a change of the magnetic response (magnetic moment, anisotropy) of the Fe film.

A particularly interesting situation is encountered when the substrate has a strong spin–orbit coupling. This is the case, e.g., with tungsten. Even this material alone may already exhibit Dirac-type band features and quantum spin mixing, as we have shown for the W(110) surface. The electrons in monolayer Fe films grown on W(110) are thus subject to both large spin–orbit (W) and large exchange interaction (Fe). Fe films can be epitaxially grown with high quality on tungsten surfaces, and the (110) orientation provides uniaxial in-plane anisotropy in the Fe films. Ultrathin Fe/W(110) may, thus, be seen as a complex quantum material system, which forces Fe to develop also topological properties via a "topological phase transition" as we will show below. Measurements were done at $T=130 \, \text{K}$.

In Fig. 12, we compare spin-resolved momentum maps for a thicker Fe film (12 monolayers) and an ultrathin one (two monolayers). Both have been magnetized to a remanent state along the -y-direction before the measurement. The data in Fig. 12(a) reflect the twofold symmetry of the {110} surface and are quite consistent with the bulk electronic structure of Fe at the Fermi level. We see predominantly majority spin bands (red) crossing E_F with distinct minority spin bands (blue), e.g., close to the \overline{H} points at $k_x = \pm 1.5 \, \text{Å}^{-1}$ (marked by rectangular frames). We note that the red and blue lines in these areas are crossing each other without sizable hybridization effects. This is due to the small SOC in bulk Fe and has been explored on the {100} surface recently.

This situation changes markedly on the two monolayers film [Fig. 12(b)]. The spin-down contribution (blue) is now more pronounced in several areas. Particularly in the rectangular frames, the intersection of the states is strongly modified. The simple crossings in Fig. 12(a) appear to be replaced by a more complex structure, with an arclike feature connecting the previous crossing points, which have now turned into Weyl points. In fact, this feature turns out to be a "Fermi arc" at the surface of the crystal. As we will discuss in the following, this Fermi arc is a consequence of the strong SOC in W(110) and the electronic interaction across the interface.

Another ingredient in the system is not directly apparent in the figures. In order for the Weyl points in the Fe layer to form, the electronic bands in Fe need to be located in a bandgap of the W crystal, i.e., at these points in k-space, there should be no electronic interaction between Fe and W states. This is indeed the case, as the strong SOC generates a projected partial bandgap along the \overline{H} - $\overline{\Gamma}$ - \overline{H} line, resembling the relativistic fundamental gap in topological insulators. $^{44-48}$

The sketch in Fig. 12(c) illustrates the origin of this arc. We start with small SOC on the left-hand side of the graph. As observed in the thick Fe film, the different spin bands can cross each other without sizable hybridization or spin-splitting. With increasing SOC, the band crossings transform into Weyl points. At the surface, the Weyl points will be connected by Fermi arcs, which also exhibit spin-splitting (right-hand side).

In contrast to the unaltered Fermi arcs in typical Weyl semimetals with time-reversal symmetry, Fig. 13 shows magnetic control of Fermi-arc states in 2MLs Fe/W(110). The Fermi arcs are theoretically characterized as true surface states with no bulk

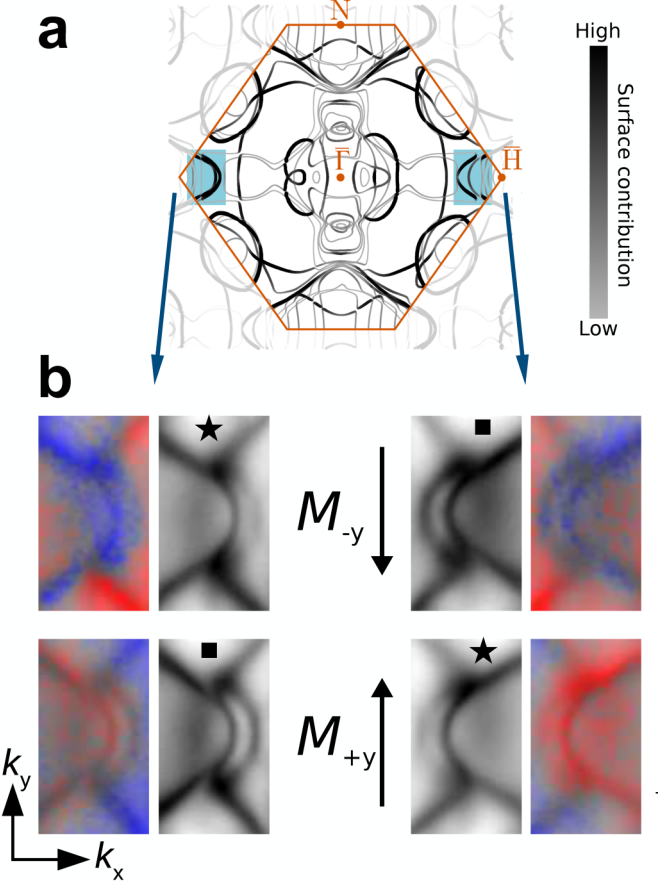


FIG. 13. Switching of Fermi arcs controlled by magnetization reversal. (a) Theoretical Fermi surface of two monolayers Fe/W(110) for in-plane magnetization \overrightarrow{M}_{-y} (Colors: degree of states' localization in Fe. Shaded regions: emergent Fermi arcs). (b) Spin-resolved (spin polarization P_y : red and blue colors, color strength: intensity) and spin-integrated surface arc states measured in the shaded regions for magnetization directions \overrightarrow{M}_{+y} and \overrightarrow{M}_{-y} (along the y direction). Shape and spin polarization of the strongly asymmetric Fermi arcs on opposite sides of the momentum map is interchange upon magnetization reversal (black stars, squares).

correspondence [see Fig. 3(a)]. The spin-resolved momentum map reveals that the shape and spin polarization of the strongly asymmetric Fermi arcs on opposite sides of the momentum map are interchanged upon magnetization reversal, as visualized by the black star and square symbols in Fig. 13(b).

Due to the breaking of TR symmetry, not only the shape but also the spin texture of the Fermi arcs is markedly asymmetric with respect to the center of the surface Brillouin zone (Fig. 14). Specifically, for the right pair of arcs, a sizable and pronounced variation of spin polarization P_x [the right panel of Fig. 14(a)] indicates considerable noncollinearity of the spin texture along the arc. This observation is consistent with the theoretical calculations presented in Fig. 14(b). The emergent monopoles in the mixed phase

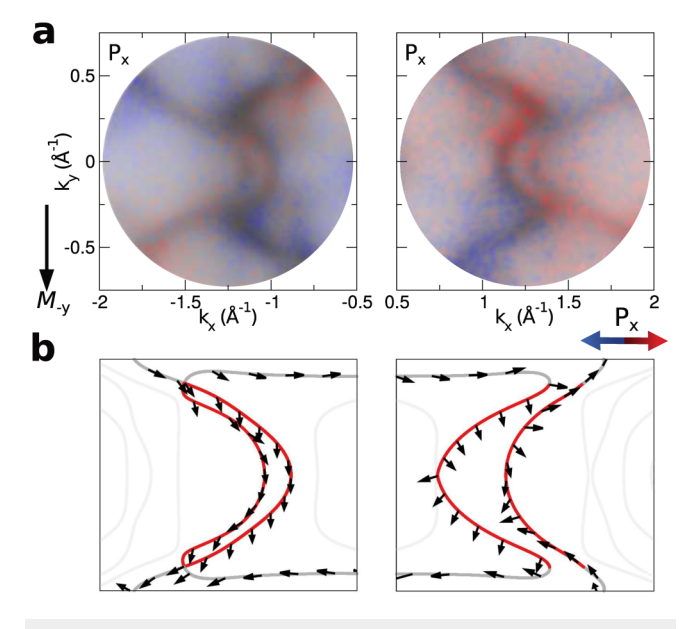


FIG. 14. Spin texture of the Fermi arcs in the 2D topological ferromagnet. (a) Spin-resolved Fermi arcs in 2 MLs Fe/W(110) measured on the left and on the right side of the momentum map (Colors: in-plane spin component along x, orthogonal to M_{-y}). Spin polarization P_x encoded the same as in Fig. 13. (b) Complete spin texture in momentum space (arrows: theory), revealing prominent noncollinearity in the Fermi arcs (red) vs the interior states (gray).

space, located near the Fermi energy, are found at the termination points where the surface arcs [red lines in Fig. 14(b)] and the interior states [gray lines in Fig. 14(b)] attach tangentially. As a result, the exotic and intricate topology in the composite phase space is the most crucial factor contributing to macroscopic effects associated with charge transport and orbital properties. This makes the emergent Fermi arcs the key element in comprehending these phenomena in 2D topological ferromagnets.

IV. CONCLUSIONS

In this contribution, we have experimentally followed the influence of symmetry reduction in selected quantum materials illustrating the changes in the electronic structures upon breaking inversion or time-reversal symmetries. The advanced technique of spin-resolved momentum microscopy is able to resolve many details of the electronic structures and also of the respective Dirac and Weyl cones forming due to symmetry reduction. The results show that even a simple ferromagnet—iron—can exhibit topological phenomena under certain conditions. These results mark a new step into the in-depth characterization of quantum materials and their related quantum phenomena.

ACKNOWLEDGMENTS

We wish to acknowledge the strong support of our colleagues V. Feyer, I. Cojocariu, and M. Jugovac during the momentum microscopy experiments carried out at the Elettra Synchrotron Facility in Trieste. We gratefully acknowledge funding by the BMBF (Grant No. 05K19PGA). We are highly indebted to J.-P. Hanke, M. Hoffmann, P. Rüßmann, G. Bihlmayer, Y. Mokrousov, and S. Blügel (FZ-Jülich) for an in-depth discussion and theoretical support. We gratefully acknowledge the contribution of high-quality NiTe2 and MoTe2 crystals, valuable support during experiments, and an in-depth discussion with our colleagues K.-H. Ou Yang, C. Jing, Y.-H. Shen, R. Sankar, F.-C. Chou, and M.-T. Lin (NTU, Taiwan), K. Ueno (Saitama University, Japan), and S. Suga (Osaka University, Japan).

AUTHOR DECLARATIONS

Conflict of Interest

The authors have no conflicts to disclose.

Author Contributions

C. Tusche: Data curation (equal); Project administration (equal); Supervision (lead); Writing - review & editing (equal). K. Hagiwara: Data curation (equal); Investigation (equal); Writing - review & editing (equal). X. L. Tan: Data curation (equal); Investigation (equal); Writing - review & editing (equal). Y.-J. Chen: Data curation (equal); Investigation (equal); Writing review & editing (equal). $\bar{\textbf{C}}$. \pmb{M} . Schneider: Conceptualization (lead); Writing - original draft (lead); Writing - review & editing (equal).

DATA AVAILABILITY

The data that support the findings of this study are available from the corresponding author upon reasonable request.

REFERENCES

1 R. Waser (ed.), Nanoelectronics and Information Technology, 3rd ed. (Wiley-VCH, Weinheim, 2012).

²A. Hirohata, K. Yamada, Y. Nakatani, I.-L. Prejbeanu, B. Diény, P. Pirro, and B. Hillebrands, J. Magn. Magn. Mater. 509, 166711 (2020).

³A.-Q. Wang, X.-G. Ye, D.-P. Yu, and Z.-M. Liao, ACS Nano 14, 3755 (2020).

⁴J. R. Schaibley, H. Yu, G. Clark, P. Rivera, J. S. Ross, K. L. Seyler, W. Yao, and X. Xu, Nat. Rev. Mater. 1, 16055 (2016).

⁵D. Go, D. Jo, H.-W. Lee, M. Kläui, and Y. Mokrousov, Europhys. Lett. 135,

⁶D. Marković, A. Mizrahi, D. Querlioz, and J. Grollier, Nat. Rev. Phys. 2, 499 (2020). 7"40 years of quantum computing," Collection in Nat. Rev. Phys. (29 November 2021) and Nat. Rev. Phys. 4, 1 (2022).

⁸E. Młyńczak et al., Phys. Rev. X **6**, 041048 (2016).

⁹E. Gorbar, V. Miransky, I. Shovkovy, and P. Sukhachov, *Electronic Properties of* Dirac and Weyl Semimetals (World Scientific, Singapore, 2021).

10 D. J. Thouless, Topological Quantum Numbers in Nonrelativistic Physics (World Scientific, Singapore, 1998).

¹¹B. Göbel, I. Mertig, and O. A. Tretiakov, Phys. Rep. **895**, 1 (2021).

 $^{\bf 12}{\rm F.}$ N. Rybakov, N. S. Kiselev, A. B. Borisov, L. Döring, C. Melcher, and S. Blügel, APL Mater. 10, 111113 (2022).

13 E. V. Chulkov et al., in Dynamics at Solid State Surfaces and Interfaces, edited by U. Bovensiepen, H. Petek, and M. Wolf (Wiley-VCH, Weinheim, 2012), Vol. 2.

¹⁴A. de la Torre, D. M. Kennes, M. Claassen, S. Gerber, J. W. McIver, and M. A. Sentef, Rev. Mod. Phys. 93, 041002 (2021).

15T. Oka and S. Kitamura, Annu. Rev. Condens. Matter Phys. 10, 387 (2019).

¹⁶M. Reutzel, A. Li, Z. Wang, and H. Petek, Nat. Commun. 11, 2230 (2020).



- ¹⁷H. Liu, J.-T. Sun, C. Song, H. Huang, F. Liu, and Sheng Meng, Chin. Phys. Lett. 37, 067101 (2021).
- ¹⁸H. Hübener, M. A. Sentef, U. D. Giovannini, and A. F. Kemper, Nat. Commun. 8, 13940 (2017).
- ¹⁹C. Tusche, Y.-J. Chen, L. Plucinski, and C. M. Schneider, e-J. Surf. Sci. Nanotechnol. 18, 48 (2020).
- **20**T. Heider *et al.*, Phys. Rev. B **106**, 054424 (2022).
- ²¹B. Krömker, M. Escher, D. Funnemann, D. Hartung, H. Engelhard, and J. Kirschner, Rev. Sci. Instrum. **79**, 053702 (2008).
- ²²C. Tusche, M. Ellguth, A. A. Ünal, C. Chiang, A. Winkelmann, A. Krasyuk, M. Hahn, G. Schönhense, and J. Kirschner, Appl. Phys. Lett. **99**, 032505 (2011).
- ²³C. Tusche, M. Ellguth, A. Krasyuk, A. Winkelmann, D. Kutnyakhov, P. Lushchyk, K. Medjanik, G. Schönhense, and J. Kirschner, Ultramicroscopy 130, 70 (2013).
- ²⁴C. Tusche, A. Krasyuk, and J. Kirschner, Ultramicroscopy 159, 520 (2015).
- 25D. Vasilyev, C. Tusche, F. Giebels, H. Gollisch, R. Feder, and J. Kirschner, J. Electron Spectr. Relat. Phenom. 199, 10 (2015).
- ²⁶H. Mirhosseini and J. Henk, Phys. Rev. Lett. **109**, 036803 (2012).
- ²⁷M. R. Scholz *et al.*, Phys. Rev. Lett. **110**, 216801 (2013).
- ²⁸M. Schüler, U. De Giovannini, H. Hübener, A. Rubio, M. A. Sentef, and P. Werner, Sci. Adv. 6, eaay2730 (2020).
- ²⁹S. Beaulieu et al., Phys. Rev. Lett. 125, 216404 (2020).
- 30 N. A. Cherepkov and G. Schönhense, Europhys. Lett. 24, 79 (1993).
- ³¹K. Hagiwara, "Spin- and orbital-dependent band structure of unconventional topological semimetals," Ph.D. thesis (University of Duisburg-Essen, 2022), see: https://doi.org/10.17185/duepublico/76864.

- ³²N. Huang, H. Deng, B. Liu, D. Wang, and Z. Zhao, Innovation 2, 100097 (2021).
- 33 R. Schoenlein, T. Elsaesser, K. Holldack, Z. Huang, H. Kapteyn, M. Murnane, and M. Woerner, Philos. Trans. R. Soc. A 377, 20180384 (2019).
- ³⁴R. Adam, C. Tusche, A. Hützen, C. Wiemann, Y.-J. Chen, M. Büscher, and C. M. Schneider, J. Large-Scale Res. Fac. 6, A138 (2020).
- **35**S. Eich *et al.*, Sci. Adv. **3**, e1602094 (2017).
- **36**P. Rüssmann, private communcation (November 15, 2023).
- 37O. J. Clark et al., Electron. Struct. 1, 014002 (2019).
- 38B. Yan and C. Felser, Annu. Rev. Condens. Matter Phys. 8, 337 (2017).
- ³⁹K. Hagiwara *et al.*, arXiv:2205.15252 (2022).
- ⁴⁰G. Schönhense, Phys. Scr. **1990**, 255 (1990).
- ⁴¹E. Młyńczak et al., Phys. Rev. B **103**, 035134 (2022).
- **42**E. Młyńczak *et al.*, Phys. Rev. B **105**, 115135 (2022).
- ⁴³Y.-J. Chen, M. Hoffmann, B. Zimmermann, G. Bihlmayer, S. Blügel, C. M. Schneider, and C. Tusche, Commun. Phys. 4, 179 (2021).
- ⁴⁴Y.-J. Chen, J.-P. Hanke, M. Hoffmann, G. Bihlmayer, Y. Mokrousov, S. Blügel, C. M. Schneider, and C. Tusche, Nat. Commun. 13, 5309 (2022).
- ⁴⁵K. Miyamoto, A. Kimura, K. Kuroda, T. Okuda, K. Shimada, H. Namatame, M. Taniguchi, and M. Donath, Phys. Rev. Lett. 108, 066808 (2012).
- 46 D. Kutnyakhov et al., Sci. Rep. 6, 29394 (2016).
- ⁴⁷A. Varykhalov, D. Marchenko, J. Sánchez-Barriga, E. Golias, O. Rader, and G. Bihlmayer, Phys. Rev. B 95, 245421 (2017).
- 48 H. J. Elmers et al., J. Phys.: Condens. Matter 29, 255001 (2017).